ARL-TR-9075 ● SEP 2020

DEVCOM ARMY RESEARCH LABORATORY

Development of Micro-indentation Tool for In-situ Mechanical Testing under Microwave Fields

by Selva Vennila Raju, Daniel Shreiber, John Pittari, Brian M Powers, and Raymond E Brennan

NOTICES

Disclaimers

The findings in this report are not to be construed as an official Department of the Army position unless so designated by other authorized documents.

Citation of manufacturer's or trade names does not constitute an official endorsement or approval of the use thereof.

Destroy this report when it is no longer needed. Do not return it to the originator.

ARL-TR-9075 ● SEP 2020

Development of Micro-indentation Tool for In-situ Mechanical Testing under Microwave Fields

Selva Vennila Raju
Oak Ridge Associated Universities

Daniel Shreiber, John Pittari, Brian M Powers, and Raymond E Brennan
Weapons and Materials Research Directorate, CCDC Army Research Laboratory

REPORT DOCUMENTATION PAGE

Form Approved
OMB No. 0704-0188

1. REPORT DATE *(DD-MM-YYYY)*	2. REPORT TYPE	3. DATES COVERED (From - To)
September 2020	Technical Report	October 2017–September 2020

4. TITLE AND SUBTITLE
Development of Micro-indentation Tool for In-situ Mechanical Testing under Microwave Fields

5a. CONTRACT NUMBER
W911NF-16-2-0050

5b. GRANT NUMBER

5c. PROGRAM ELEMENT NUMBER

6. AUTHOR(S)
Selva Vennila Raju, Daniel Shreiber, John Pittari, Brian M Powers, and Raymond E Brennan

5d. PROJECT NUMBER

5e. TASK NUMBER

5f. WORK UNIT NUMBER

7. PERFORMING ORGANIZATION NAME(S) AND ADDRESS(ES)
CCDC Army Research Laboratory
ATTN: FCDD-RLW-ME
Aberdeen Proving Ground, MD 21005

8. PERFORMING ORGANIZATION REPORT NUMBER
ARL-TR-9075

9. SPONSORING/MONITORING AGENCY NAME(S) AND ADDRESS(ES)

10. SPONSOR/MONITOR'S ACRONYM(S)

11. SPONSOR/MONITOR'S REPORT NUMBER(S)

12. DISTRIBUTION/AVAILABILITY STATEMENT
Approved for public release; distribution is unlimited.

13. SUPPLEMENTARY NOTES
ORCID ID(s): Raju 0000-0003-2532-8654; Shreiber 0000-0002-4915-5471; Pittari 0000-0001-9611-3138; Powers 0000-0002-9579-1006; Brennan 0000-0001-5421-4467

14. ABSTRACT
A novel in-situ indentation technique was developed to study mechanical properties of materials under 2.45-GHz single-mode microwave (MW) fields. The ultimate goal of the investigation was to establish viability of the application of MW fields to a two-phase material, where one phase was an MW susceptor, and the matrix was transparent to the MW field. In this scenario, the hypothesis was that the stress associated with the coefficient of thermal expansion mismatch between the second phase particle and the matrix will yield better toughness properties. A Knoop indenter and sample loading assembly were designed to indent samples at high temperatures under MW fields, yielding a first system of its kind. Several indentation tests were performed on conventionally sintered alumina (Al_2O_3):10 wt% nickel ferrite ($NiFe_2O_4$). A sample loading procedure and an indentation testing procedure under MW fields were established. For the first time, in-situ indentation was achieved at temperatures up to 400 °C under a 2.45-GHz single-mode MW field. A comparison was made of indentations under no applied field and progressively increasing fields (resulting in increased sample temperatures) at 100% H-field conditions. Knoop hardness and toughness of Al_2O_3:10 wt% $NiFe_2O_4$ composites were compared with and without the application of MW fields. The designed system can be used for other applications, such as investigation of mechanical properties of ceramic materials at high temperatures.

15. SUBJECT TERMS
single-mode microwave, ceramic processing, energy coupled to matter, sintering

16. SECURITY CLASSIFICATION OF:			17. LIMITATION OF ABSTRACT	18. NUMBER OF PAGES	19a. NAME OF RESPONSIBLE PERSON
a. REPORT	b. ABSTRACT	c. THIS PAGE			Selva Vennila Raju
Unclassified	Unclassified	Unclassified	UU	31	19b. TELEPHONE NUMBER (Include area code) (410) 278-3222

Contents

List of Figures

List of Tables

Acknowledgments

The author Selva Vennila Raju would like to thank the following US Army Combat Capabilities Development Command (CCDC) Army Research Laboratory (ARL) personnel:

- Victoria Blair for the valuable help in establishing the process to fabricate the pellets used in this study;
- Steve M Kilczewski for timely help with cold isostatic pressing of the samples;
- Michael Kornecki for his valuable help and useful discussions; and
- Bobby Gamble for surface polishing of the alumina rods.

We offer special thanks to David M Gray for his valuable help in remodeling the mounting stage of the single-mode microwave system to improve the stability of the system, which was critical for indentation setup and ongoing efforts to incorporate the Instron component. We want to also thank Jerry LaSalvia and Jeff Swab for valuable advice throughout the duration of the project.

SV Raju was sponsored by the CCDC Army Research Laboratory under Cooperative Agreement No. W911NF-16-2-0050. The views and conclusions contained in this document are those of the authors and should not be interpreted as representing the official policies, either expressed or implied, of ARL or the US Government. The US Government is authorized to reproduce and distribute reprints for Government purposes not withstanding any copyright notation herein.

1. Introduction

Processing materials under electromagnetic (EM) fields influences numerous material parameters, including grain size, mobility, defect energy, microstructure, diffusion coefficients, and phase formation. Indentation under elevated temperatures, as well as various electric "E" and magnetic "H" field ratios (E/H), is crucial to understanding mechanical responses and tunability of material properties.[1] Very little experimental work has been reported on these properties due to a lack of instrumentation,[1–4] and no related research has been performed under microwave (MW) fields. Materials absorb MW energy based on the nature of their polarization, electric permittivity, magnetic permeability, and electrical conductivity behavior, as they rapidly heat to high temperatures within minutes, leading to changes in their mechanical behavior. For energy-coupled-to-matter (ECM) research, the majority of work has focused on novel processing of materials, with limited emphasis on applied EM fields as a function of mechanical response in materials. In this proposed research, the fracture resistance of ceramics in the presence of MW fields is studied. A fundamental question is whether or not the fracture resistance of ceramics can be enhanced in the presence of MW fields, and if so, by what mechanisms and contributing factors.

The main subject of this report is the design and implementation of a tool capable of measuring and comparing hardness and indentation toughness of materials in the presence of MW fields. Also, this novel device is required to address the primary question posed in this work, and as described in the previous paragraph. In general, the focus on fracture mechanics is two-fold. First, fracture mechanics is an important field of knowledge for understanding the majority of ceramic failures under working conditions, and fracture toughness is dependent on the stress states within the grains and grain interfaces of ceramic materials.[5,6] Second, the rapid heating of ceramics via MWs alters the microstructure of the material, and these processes are linked to both nonuniform heating of the material and the formation of cracks and flaws within the material. It is important to gain a better understanding of the external field-dependent mechanical deformation behavior of such materials at high temperatures, as the proposed mechanisms could serve as a novel way to enhance fracture toughness in ceramic armor.

Alumina (Al_2O_3), a widely used industrial material for its high strength, chemical compatibility, and high electrical and thermal insulating properties, has been chosen for this study. It was shown that incorporation of a ductile metal into the hard ceramic matrix considerably improved fracture toughness of Al_2O_3-aluminum (Al), Al_2O_3-iron (Fe), and Al_2O_3-titanium (Ti) cermets after pressureless sintering for 1 h at 1500 °C.[7] Al_2O_3 has been selected to be the matrix of the composite

because it is almost transparent to external EM field at room temperature. Nickel ferrite ($NiFe_2O_4$) has been selected as a second phase that will be responsible for enhancing the fracture toughness of the composite upon application of external EM fields. In addition, from our previous studies on the sintering behavior of Al_2O_3 with $NiFe_2O_4$ and cobalt ferrite ($CoFe_2O_4$) additives, $NiFe_2O_4$ was found to be a good MW absorber, with phase stability over a wide range of E/H MW fields.[8] For these reasons, indentation of Al_2O_3 containing 10 wt% $NiFe_2O_4$ was conducted under MW fields, and the results are presented.

1.1 Hypothesis

In this research, the aim is to study the fracture resistance of ceramics under the presence of MW fields while determining the fundamental mechanisms and appropriate length scales. The goal is to develop a tool that is capable of determining the indentation toughness of the material using an in-situ MW micro-indentation technique and validate the results by comparing with results from a standard Knoop indenter. For this purpose, an indenter tool is required that possesses the following characteristics: 1) noncoupling (negligible/transparent) under MW fields, 2) high strength at high temperatures to sustain the applied load, and 3) low coefficient of thermal expansion (CTE) to sustain indentation tests at high temperatures. Therefore, there is a need to develop an indentation technique, fixtures, and specimen geometries for measuring the temperature and fracture resistance of ceramics inside the MW chamber. Additionally, preliminary modelling methods will help to understand the underlying mechanisms and their effect on particle size, temperature, and load.

1.2 Preliminary Modelling Study

The effect of particle size and temperature change on the stress intensity factor of a crack interacting with a system of particles (singularity elements) was determined using numerical modelling. In determining the effects the expansion of particles will have on the surrounding material, two configurations were studied. The first configuration was an isolated spherical particle in an infinite medium undergoing a uniform temperature change. As the particle expands, it will induce stresses in the surrounding matrix, which can cause cracking.[9] The stress of highest interest is the hoop (tangential) stress, σ_θ, in the matrix, since it is tensile and leads to cracking. For this configuration, the stress is

$$\sigma_\theta^M = \frac{\alpha^I E^I E^M \Delta T}{[E^I(1+\nu^M)+2E^M(1-2\nu^I)]}\left(\frac{a^3}{r^3}\right) \quad (1)$$

where α^I is the coefficient of thermal expansion for the inclusion, and E^I and ν_M are the Young's modulus and Poisson's ratio for the inclusion. E^M and ν^M are the Young's modulus and Poisson's ratio for the matrix, ΔT and a are the temperature change and radius of the inclusion, and r is the radial distance from the center of the inclusion. The maximum stress in the matrix occurs at the interface with the inclusion at $r = a$. The temperature change in the inclusion that can induce cracking is determined by setting σ_θ^M equal to the failure stress of the matrix and rearranging Eq. 1 such that

$$\Delta T = \frac{[E^I(1+\nu^M)+2E^M(1-2\nu^I)]\sigma_{fail}}{\alpha^I E^I E^M} \tag{2}$$

For a system with a SiC particle in an Al_2O_3 matrix, the properties of the materials are tabulated in Table 1. Using Eq. 2, the maximum temperature that silicon carbide (SiC) particles can reach before causing failure in the Al_2O_3 is 623 °C.

Table 1 Material properties for SiC and Al_2O_3

Material property	SiC	Al_2O_3
E (GPa)	410	300
ν	0.14	0.21
α (C^{-1})	4.0×10^{-6}	. . .
σ_{fail} (MPa)	. . .	330

The second configuration was used to investigate whether expanding particles could inhibit a crack. A 2D model was created in ABAQUS[10] with a group of four particles near a crack tip. A schematic of the model is shown in Fig. 1, which approximates a compact tension fracture test. ABAQUS uses the J-integral[11,12] method to calculate the Mode I stress intensity factor, K_I, which is a measure of the strength of the crack. K_I is defined by

$$K_I = \lim_{r \to 0} \sqrt{2\pi r}\, \sigma_{yy} \tag{3}$$

where r is the distance from the crack tip, and σ_{yy} is the stress in the direction perpendicular to the crack tip. The J-integral method uses a contour integral, which surrounds the crack tip, and is defined as

$$J = \int_\Gamma (W dy - T_i \frac{\partial u_i}{\partial x_i})\, ds \tag{4}$$

where Γ is the contour path, W is the strain energy density, T_i is the surface traction, and u_i is the displacement vector. The relationship to K_I is

$$\mathrm{J} = \frac{1-\nu^2}{\mathrm{E}} \mathrm{K_I^2} \tag{5}$$

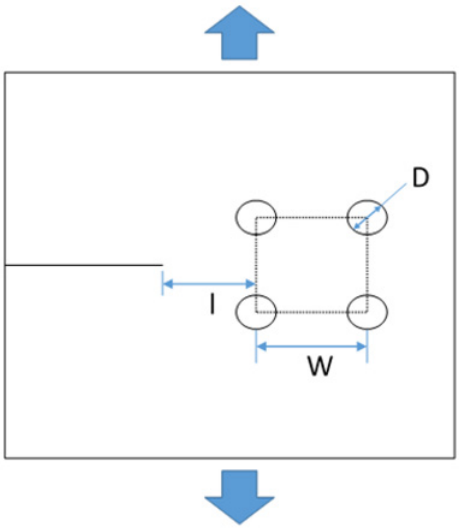

Fig. 1 Configuration of a compact tension fracture test with inclusions

The J-integral is formulated for homogenous materials. The implications for this study is that the crack tip cannot be too close to an inclusion, since the contour cannot cross multiple materials. This limits the inclusions from being too closely packed, as the calculated K_I values will be inaccurate.

The parameters varied for the four inclusion configurations were the temperature change in the particles, ΔT, the particle diameter, D, and the distance from the crack tip to the particle group, l. The area fraction, A_f, of the particle array is held constant at a value of 0.3 and is used to determine the particle spacing, w. The area used for area fraction calculation is denoted by the square of dimension w, which connects the centers of the particles in Fig. 1. A_f is calculated by

$$A_f = \frac{\pi D^2}{4w^2} \tag{6}$$

Since A_f is held constant, larger-diameter particles have a larger particle spacing. Three particle sizes were studied with diameters of 50, 60, and 80 μm, respectively, which approximately corresponded to the diameters of SiC particles. Three temperature changes were also studied, including ΔT= 0, 250, 500 °C. The distance, l, was varied by moving the inclusions closer to the crack tip. This avoided the issue of K_I varying because of the change in crack length. The K_I value for the case of a pure matrix with no temperature change was determined as the baseline for comparison and is denoted as K_0.

Figure 2 shows the results of the numerical study. The normalized stress intensity factor, K_1/K_0, is plotted versus the normalized distance from the crack tip, $\frac{2l}{D}$. When the normalized distance is positive, the crack tip is to the left of the inclusions, as

in Fig. 1. When the normalized distance is negative, the crack tip is inside the box made by the inclusions, and at zero, the crack tip is in the line with the centers of the inclusions on the left. The bold line at $K_1/K_0 = 1$ is the baseline case of no inclusions. A K_1/K_0 value above this line means the crack tip is stronger, and below this line means the crack tip is weaker. In Fig. 2, the line color corresponds to temperature change, in which symbol and line type correspond to particle size.

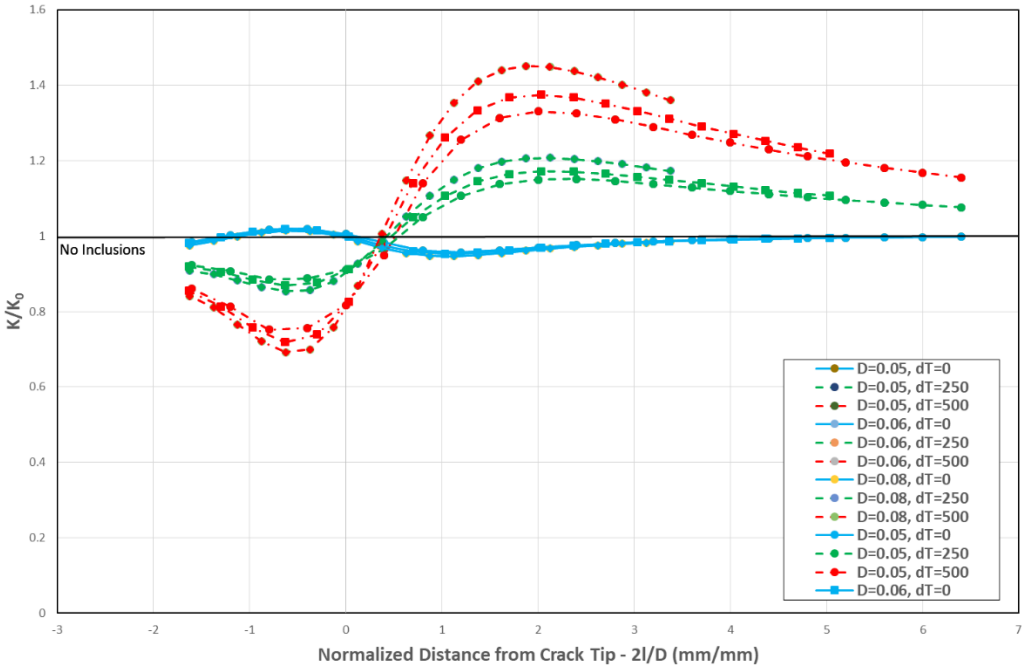

Fig. 2 The normalized stress intensity factor, K_1/K_0, plotted as a function of the normalized distance, $2l/D$, from the crack tip

Figure 2 shows that as the crack tip gets farther from the inclusions, the stress intensity facture trends toward the case of no inclusions for all particle size and temperature combinations, which is to be expected. For all cases, increasing the temperature increases the effect of inclusions on the crack tip, both for better and worse. Near the inclusions, for $2l/D > 0$, there is a small benefit, where the K_1/K_0 is below 1 for the smallest particle size, 50 μm. For the larger particles, the addition of the inclusions make the crack tip stronger for all temperature changes, with the highest temperature change and largest particle being the worst case examined. For $2l/D < 0$, the inclusions have a small detrimental effect for the 50-μm particles, where K_1/K_0 is slightly above 1. When the crack tip is surrounded by 60- and 80-μm particles, the strength of the crack tip decreases with $K_1/K_0 < 1$. The best-case scenario is when the crack tip is surrounded by the largest particles, and the temperature change remains highest.

These results suggest that if the particles are spaced closely enough so that the crack tips are always surrounded by particles, there is some benefit to the inclusions. If

the particle spacing becomes too large, the benefits will be lost, and the addition of the particles will make the cracks more likely to propagate.

2. Experimental Procedures

2.1 Technical Challenges and Materials Selection

Ceramic materials can fail catastrophically under impact loads, and their strength decreases at elevated temperatures. To understand and improve the strength of a two-phase system at these temperatures (where the temperature increase is mainly due to the heating of second-phase particles), we need to understand crack propagation behavior and indentation toughness at high temperatures and varying loads. To investigate this, microstructural imaging of MW field–induced crack propagation in commercial Al_2O_3 was studied. The goal of this approach was to determine the feasibility of comparing fracture toughness values in baseline Al_2O_3 samples and Al_2O_3 samples containing second-phase particles. In this experiment, a few hundred micron–length crack was deliberately created on a solid commercial Al_2O_3 pellet. This pellet was placed into the 2.45-GHz single-mode MW chamber in the configuration shown in Fig. 3a. Sintered SiC-N plate larger than the sample diameter was used as the susceptor material. Induced crack propagation on the sample surface was monitored and recorded during heating and cooling cycles using a high magnification optical camera with a 1.1-µm resolution.

Optical images of the pre-crack in the Al_2O_3 sample were recorded at high temperatures under MW fields, but the change in crack length was not notable, as shown in Fig. 3b. Resolution of the microscope was not high enough to study the crack propagation. Magnetron vibrations were also high and altered the image when the MW field was applied. This approach of comparative crack propagation monitoring was not deemed feasible for the purpose of this research. Therefore, to improve sample responsiveness to the MW field, Al_2O_3 with 10% $NiFe_2O_4$ by weight was selected for further experimentation. This study included in-situ indentation of the samples with and without the presence of an MW field. Further, the choice of $NiFe_2O_4$ as an internal susceptor was based on previous studies comparing MW absorption for various ferrites in Al_2O_3.[8]

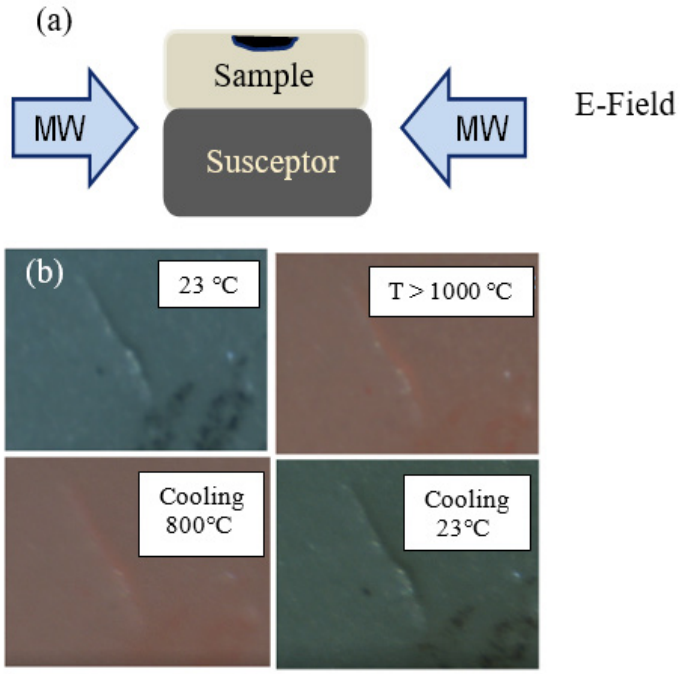

Fig. 3 a) Schematic representation of Al_2O_3 (specimen) and susceptor configuration under MW field. b) Microstructural image of the crack during heating and cooling cycles recorded using a high-resolution camera.

2.2 Material Preparation and Characterization

The nickel ferrite powders were synthesized via solid-state reaction of iron oxide (Fe_2O_3) and nickel oxide (NiO). Stoichiometric ratios of Fe_2O_3 and NiO were ball-milled in isopropanol with Al_2O_3 milling media for approximately 72 h to enable a homogenous distribution of $NiFe_2O_4$ particles. After drying the resultant slurry, the powder was air-fired to 1100 °C at 10 °C/min heating rate for 1 h to obtain the $NiFe_2O_4$ phase. Further, the composite Al_2O_3 powder with 10 wt% Fe_2O_3 was loaded into a Nalgene bottle with isopropanol and Al_2O_3 milling media, and ball-milled for approximately 48 h. The milled powder was dried in a vacuum oven. The resultant dried powder was then calcined at a rate of 5 °C/min up to 450 °C for an hour to remove any traces of Nalgene particles from the milling process. Figure 4 shows the microstructure and energy dispersive spectroscopy (EDS) of the Al_2O_3:10 wt% $NiFe_2O_4$ ball-milled powder. The calcined powder was then pressed into 13-mm pellets at 24.3 MPa using a 13-mm stainless steel die. These pellets were cold isostatically pressed up to 206 MPa for 30 s. The pellets were then sintered in an air-fired furnace at 10°C/min up to 1500 °C and held for 2 h. X-ray diffraction data collected using Cu K-alpha wavelength 1.5406 Å, as shown in Fig. 5, confirmed the presence of Al_2O_3 and $NiFe_2O_4$ phases.

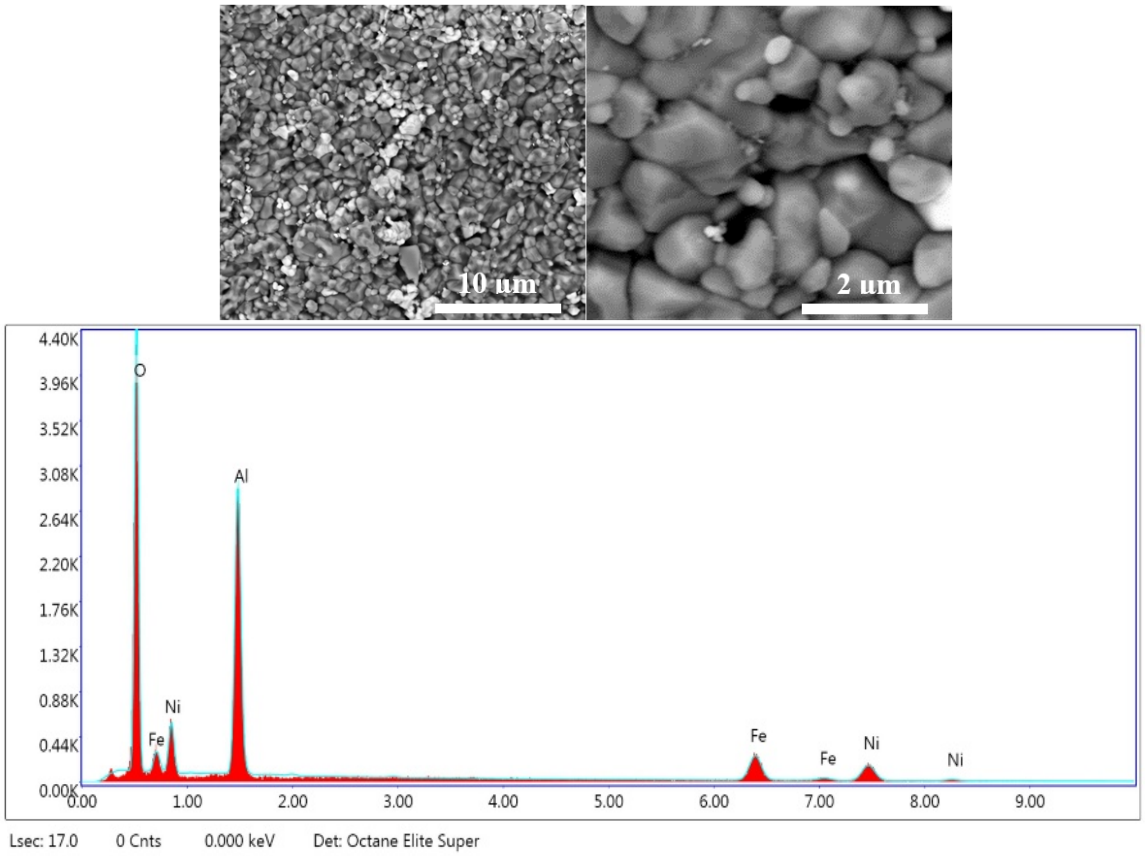

Fig. 4 Microstructure and EDS of ball-milled Al_2O_3:10 wt% $NiFe_2O_4$ powder

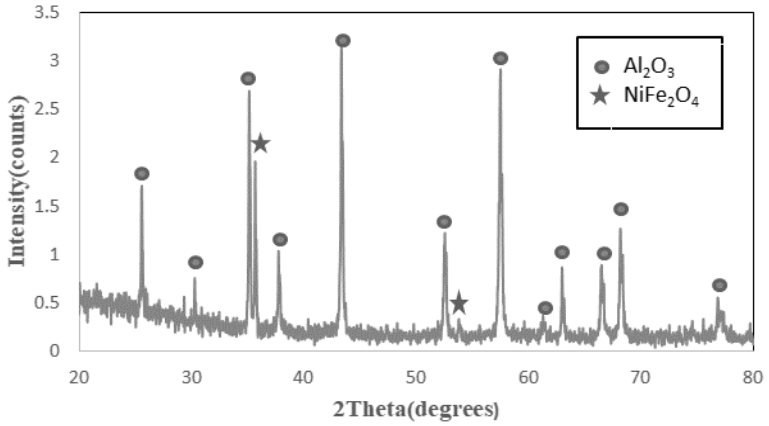

Fig. 5 X-ray diffraction data of green body collected using a Bruker AXS D8 diffractometer at Cu K-alpha wavelength 1.5406 Å from 20° to 80° 2θ using a scintillation detector

Densities of the green pellet was 1.83 g/cm^3 measured geometrically and the final sintered pellet measured using Archimedes' method was found to be 1.83 and 3.833 g/cm^3, with relative densities of 44% and 94%, respectively.

2.3 Single-Mode MW Assembly

A 2.45-GHz single-mode MW system, with 2 kW of adjustable MW energy, was used for sintering the samples shown in Fig. 6. A single-mode MW consists of a single standing wave formed within a specially designed cavity. As opposed to the standard multimode MW system, it offers the possibility of heating materials under varying E/H ratio field conditions.[13] MW absorption of the selected samples depends on dielectric and magnetic losses, and coupling varies as a function of the field. Sample mounting assembly parts were fabricated out of a high-purity porous Al_2O_3 SALI board from ZIRCAR Ceramics Inc. (Florida, New York). A dual-color pyrometer was used for measuring sample temperatures in the range of 700 to 1800 °C.

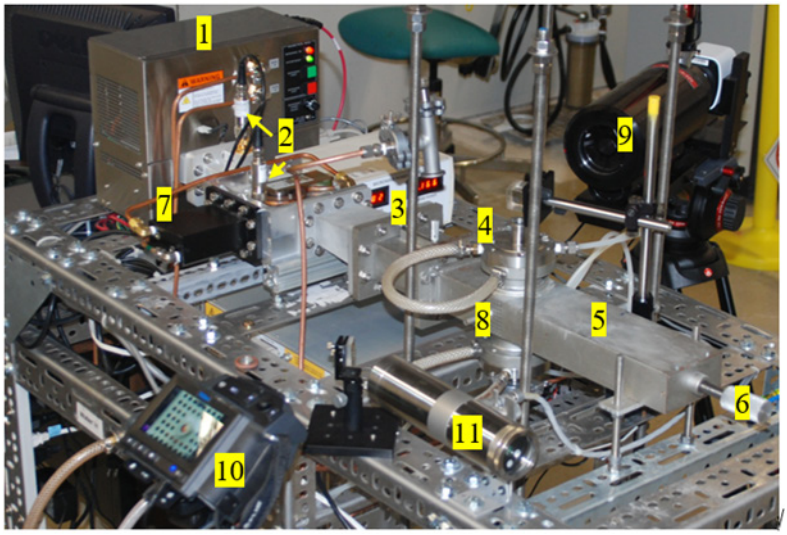

Fig. 6 Experimental setup of 2.45-GHz single-mode MW system, including 1) MW generator, 2) MW sensor, 3) iris, 4) sample chamber, 5) waveguide, 6) tuner, 7) water load, 8) optical port, 9) high-resolution camera, 10) forward-looking infrared camera, 11) two-color pyrometer

The sintered Al_2O_3:10 wt% $NiFe_2O_4$ pellet had a mass of approximately 1 g and was polished to mirror finish (1 μm). The sample was loaded into the chamber with the polished surface facing the indenter tip assembly. The iris and plunger positions of the single-mode MW were set at 100% H-field condition. Initially, the MW power was increased to 11% for the power supply, which was the minimum power to initiate MW emission. In this stage, the sample chamber was tuned by adjusting the plunger so that the reflected power was minimized. When the sample began to absorb MW power, the temperature rapidly increased. There is an optimal temperature at which the CTE mismatch between the selected particle and matrix was desired to generate a high enough stress to work against propagating crack field. Indentation tests were performed as soon as the sample reached the desired temperature. If the temperature was too high, the particle/matrix interface softened,

and the resulting CTE mismatch stress was diminished. Alternatively, the particle/matrix interface could develop additional cracks at high temperature, reducing toughness of the sample. Therefore, we targeted mechanical property measurements on Al_2O_3:10 wt% $NiFe_2O_4$ 500 °C. The temperature of the sample was determined from an independent experiment using a K-type thermocouple on a sintered Al_2O_3:10 wt% $NiFe_2O_4$ pellet under a MW field without the indenter tip assembly. Several indentation tests were performed. Depending on the coupling of the sample with the MW, the power was further increased in steps of 1%, and the waveguide was continuously tuned until the sample reached the maximum possible steady-state temperature.

2.4 Design of Indenter

There are several issues and challenges to consider when designing the indenter for use under MW fields (in contrast to the standard commercial micro-indenters). This leads to new requirements, including 1) fabrication of nonmetallic indenters, unlike the typical commercial indenters shown in Fig. 7a, 2) high-strength materials at high temperatures during in-situ testing, 3) piston and bonding materials that are transparent or very low MW absorbers at 2.45 GHz, 4) low thermal expansion and thermal conductivity materials, and 5) piston and bonding materials that can handle the rapid heating conditions from MW fields. In a standard indenter, the diamond is typically mounted to the stainless steel piston and cut to the appropriate shape while attached to the metal base, as it dissipates heat generated by the cutting step. In this case, the diamond had to be cut before it was attached to the Al_2O_3 piston, as the Al_2O_3 material was unable to efficiently dissipate heat from the cutting step.

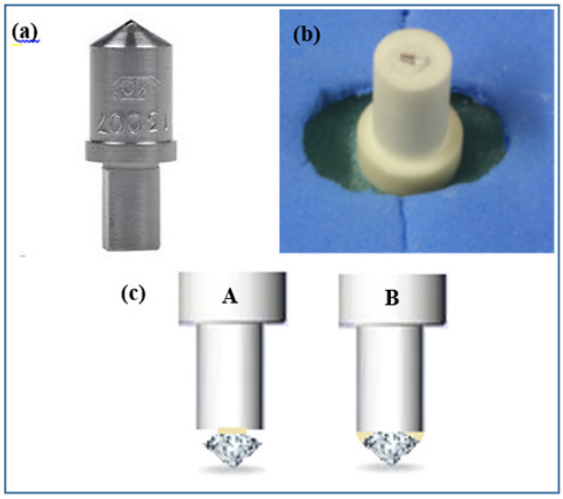

Fig. 7 a) Standard metal indenter with piston. b) Ceramic piston and indenter designed for use under MW fields (fabricated by Delaware Diamond Knives & Tools, Inc.). c) Al_2O_3 cement (represented in yellow) between diamond and piston (part A) and diamond directly in contact with piston and cement around diamond (part B).

High-purity solid Al_2O_3 (Alcoa A16), a low-MW absorber possessing high strength at high temperatures, was used for the piston design. The surface of the piston required tolerances of ±0.0001 inches at the top and bottom parallel ends. A 0.25-inch-diameter piston with a support head and a Knoop diamond micro-indenter, fabricated by Delaware Diamond Knives & Tools, Inc., was bonded to the Al_2O_3 piston using high-temperature Al_2O_3 cement (Res Bond 940HT), as shown in Fig. 7b.

During initial attempts, Al_2O_3 cement was applied between the diamond and the Al_2O_3 piston, as shown in Fig. 7c (part A), which led to the failure of the diamond upon heating in the MW chamber. This may have been due to CTE mismatch between the diamond and the Al_2O_3 cement, which may have expanded and caused misalignment. Therefore, the bonding configuration was modified to the one depicted in Fig. 7c (part B), in which several indentations were executed before the setup eventually failed.

2.5 Details of Pressure Assembly

Al_2O_3 rods 1 inch in diameter were used to support and extend the piston to both the top and bottom of the hydraulic press, with details described in the following. Initial indentation experiments were carried out at room temperature in the MW chamber. Figure 8 shows the indentation assembly loaded and integrated with an H–frame-type hydraulic press (ENERPAC). An image containing various components of the indentation assembly is shown in Fig. 9.

Locking collars were used at the top and bottom to secure the rods for convenient assembly and mounting of the sample. The height of the Al_2O_3 and steel extension rods at the top and bottom ends was chosen so that the sample and the indenter were aligned to the center of the optical port, or half the height of the waveguide.

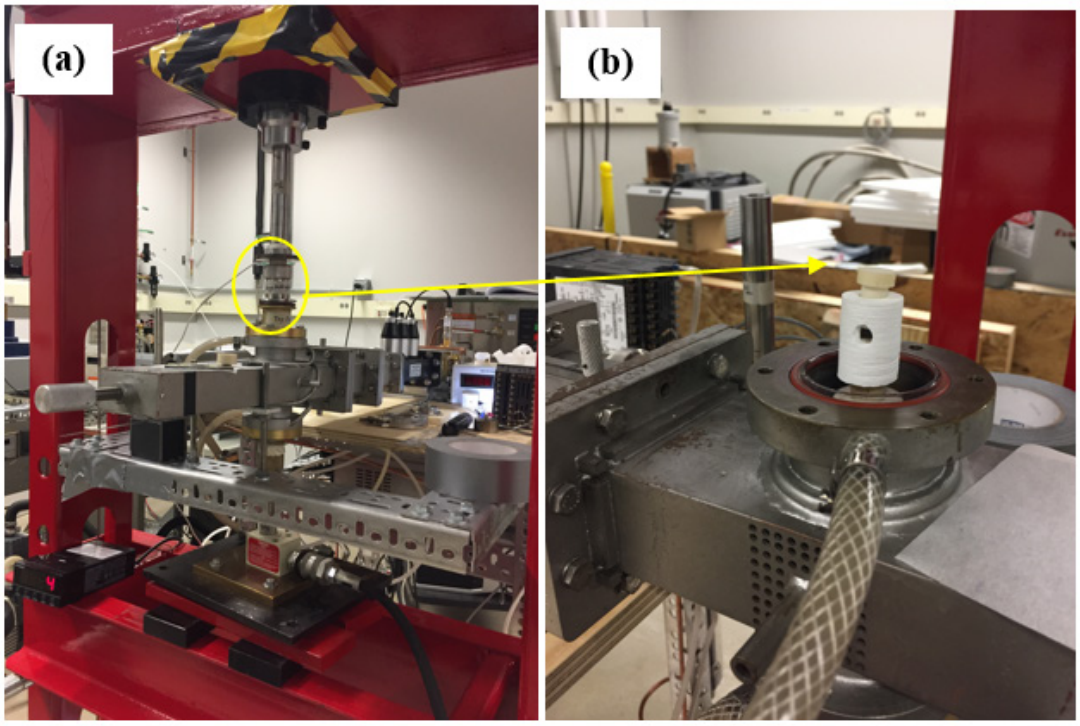

Fig. 8 a) MW indentation assembly integrated with the 2.45-GHz single-mode MW and the hydraulic press. b) Sample mounted with indenter piston in a porous Al_2O_3 enclosure.

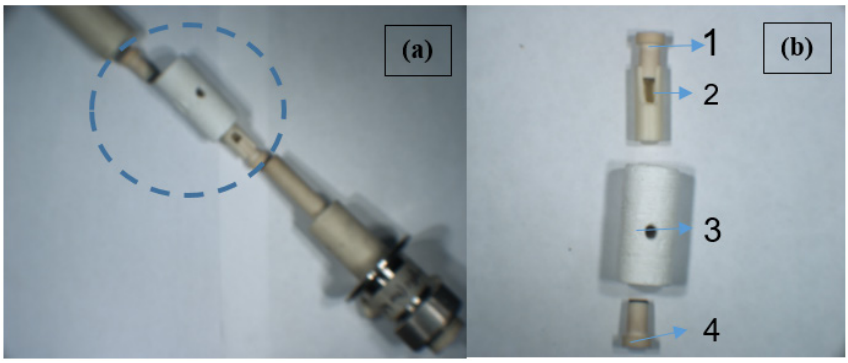

Fig. 9 a) MW indentation assembly. b) Expanded view of the dashed circle region, including 1) Al_2O_3 piston with diamond indenter, 2) Al_2O_3 sleeve, 3) porous Al_2O_3 sleeve with optical window, 4) sample mounted on Al_2O_3 piston.

2.6 Procedure for In-Situ Indentation under MW Fields

A schematic representation of the indentation assembly under MW fields is shown in Fig. 10.

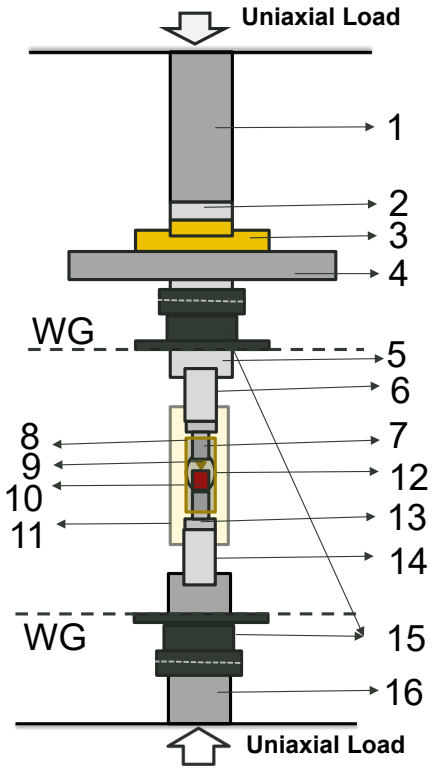

Fig. 10 Schematic representation of MW indentation assembly. Dashed lines representative of waveguide (WG) top and bottom edges. The components of the assembly consist of the 1) top steel rod, 2) Al_2O_3 support disc, 3) load cell, 4) steel support plate, 5) Al_2O_3 rod with counter bolt insert for part #6, 6) Al_2O_3 insert, 7) top Al_2O_3 piston, 8) solid Al_2O_3 sleeve, 9) diamond indenter, 10) sample, 11) porous Al_2O_3 sleeve, 12) optical view port for pyrometer, 13) bottom Al_2O_3 piston, 14) bottom Al_2O_3 rod, 15) steel clamp locking mechanism, and 16) bottom steel mounting rod.

The assembly was mounted on an H-frame hydraulic press, and uniaxial pressure was applied to determine suitable load conditions for the sample. A procedure was developed to indent the specimen symmetrically without any scratches, as described in the following steps:

1) Mount the top steel rod (#1) on the hydraulic press, inserting all the way in (flush) and securing by tightening the screw.

2) Insert the bottom steel rod (#16) into the MW chamber from below and secure it using the steel clamp locking mechanism (#15). Stack up the bottom Al_2O_3 rod (#14).

3) Assemble the bottom piston (#13) inside the solid Al_2O_3 sleeve (#8) and place it on the top Al_2O_3 rod (#14) with the supporting porous Al_2O_3 sleeve (#11).

4) Place the sample (#10) flat on top of the bottom piston with the polished sample surface at the top. Insert the top Al_2O_3 piston with the diamond indenter gently, so that the indenter tip is held just above the sample with the porous Al_2O_3, as a function of its variable inner diameter design. Take care not to apply force on the sample. The assembly described in step 4 and 5 is hereafter referred to as the indenter–sample puck. Rest the indenter–sample puck on the bottom Al_2O_3 rod (#14).

5) Unlock the bottom steel clamp locking mechanism (#15) and mark a line on the lower edge of the rod after aligning the sample with the optical view port (#12).

6) After covering the top MW brass flange, gently insert the assembly into the porous Al_2O_3 sleeve (#9) and clamp down using the steel clamp (#15).

7) Assemble the Al_2O_3 rod (#5) with the counter bolt insert (#6) and secure using the top steel clamp (#15).

8) Use the machined Al_2O_3 insert (#5) to press fit with (#6) to avoid accidental contact with the indenter piston during assembly.

9) Place the load sensor assembly (#2, #3, #4) on the top Al_2O_3 piston insert (#5), and pull the top steel rod (#1) down until it just touches the Al_2O_3 support disc (#2) and holds the load sensor assembly in place. Measure the applied load using the miniature compression load cell model LC321-750 from Omega Engineering (Norwalk, Connecticut), connected through DP41-B meter read-out.

10) Pump the pressure until the desired height marked on the steel rod (#11) is reached. Monitor the sample view port and align the Al_2O_3 piston with the counter bolt insert (#5) in contact with the top of the indenter (#6).

11) Release the O-ring on the steel flange before initiating indentation.

12) The assembly is ready for indentation under MW fields. Turn the MW ON and increase the power setting to the desired power percentage or sample temperature.

13) After indenting, tighten the O-ring so the counter bolt (#5) does not drop upon release.

2.7 Standard Knoop Indentation Test

The Knoop hardness is defined as the ratio of the applied load, F, divided by the projected area, A, of the indent. The Knoop hardness number is given by Eq. 1[14]:

$$H_K = \frac{F_{(kg)}}{A_{(mm)^2}} \sim 14.229 \frac{F}{L^2} \quad (7)$$

where L is the length of the longest diagonal (in millimeters), and F is originally measured in kilogram-force. If F is measured in newtons, Eq. 7 should be divided by 9.8065.

Standard Knoop indentation tests were carried out on polished Al_2O_3:10 wt% $NiFe_2O_4$ samples at ambient temperatures using a standard Knoop indenter (Instron/Wilson Tukon 2100B). Knoop indentation was made by indenting at a rate of 10 s/Ns to reach the maximum applied load with a hold time of 15 s at the maximum load before unloading. The indentation results are presented in the following section under Table 2.

3. Results and Discussion

The following challenges were overcome in designing the instrumentation for indentation under MW fields. A ceramic indenter was designed for compatibility with MW fields. A diamond Knoop indenter with a punch assembly was designed and fabricated by Delaware Diamond Knives/Applied Diamond, Inc. Figure 7c shows the position of ceramic cement that was originally used in configuration A, in which cement was applied between the diamond and the piston. Potential issues with diamond indenter damage due to CTE mismatch were overcome by bonding the diamond as in configuration B, in which the diamond was in direct contact with the piston, and the cement was applied around the diamond indenter. Asymmetric indentation due to tilting of the indenter was avoided by designing a combination of solid and porous Al_2O_3 sleeves, as shown in Fig. 9. Porous sleeves were also designed with integrated optical windows to allow sample temperature measurements with an optical pyrometer. Procedures for indentation testing were established to avoid multiple indents/damage to the sample prior to the actual indentation test. An H-frame hydraulic press was integrated for application of the load as well as stability of the pressure assembly. A procedure was successfully established for indentation under MW fields at high temperatures. The modified design enabled repeatability of symmetric indentations.

3.1 Evaluation of Specimens

Indentations produced in the absence of a field and progressively increasing field conditions (leading to increased sample temperatures) were compared, as shown in Fig. 11.

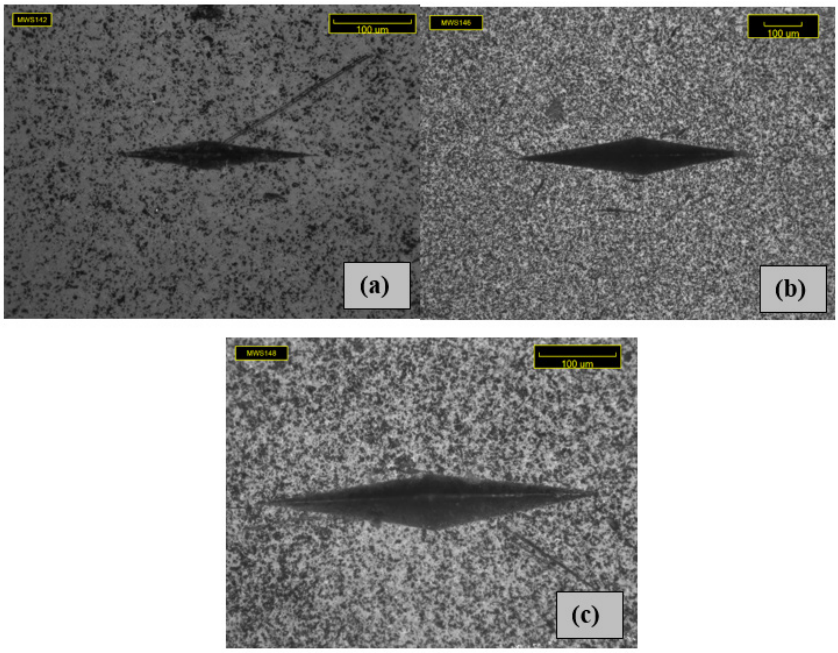

Fig. 11 Optical image of Al_2O_3:10 wt% $NiFe_2O_4$ indented a) in the absence of MW fields, b) under 11% MW field power (max power 2 kW) and 100% H-field for 2 min, yielding 90 °C effective temperature, and c) under 12% MW field power (max power 2 kW) and 100% H-field for 3 min, yielding 400 °C effective temperature

Indentation tests were conducted under 100% H-field and reduced by coupling with $NiFe_2O_4$ to study the behavior at temperatures below 500 °C. Operating at this temperature also avoided phase changes. The indented samples were allowed to undergo unassisted cooling and were recovered from the MW chamber once room temperature was reached. Measurements of the indented region were made using an optical microscope, as shown in Fig. 11.

3.2 Indentation Analysis

To validate the results, indents made at ambient temperatures with the newly developed MW indentation setup were compared to those from a standard Knoop indenter (Instron/Wilson Tukon 2100B) at ambient temperatures. Table 2 lists the values of the long diagonal length, L, applied load of the indentations, F (as measured under an optical microscope), and Knoop hardness, H_k, of Al_2O_3:10 wt% $NiFe_2O_4$ measured at room temperature using a standard Knoop indenter for various loads. For comparison, the measured diagonal length, L, and the applied load, F, were measured using both standard indentation and MW setups, as shown in Fig. 12.

Table 2 Knoop indentation values of Al_2O_3:10 wt% $NiFe_2O_4$ measured at room temperature

Run no.	Diagonal length (mm)	Load (kgf)	H_K (kgf/mm^2)
1	0.1274	1.5	1315
2	0.1517	2	1236
3	0.1629	2.5	1340
4	0.1943	3.5	1319
5	0.2168	4.5	1362
6[a]	0.2482	6.8	1572

[a] Measured with the MW indentation setup

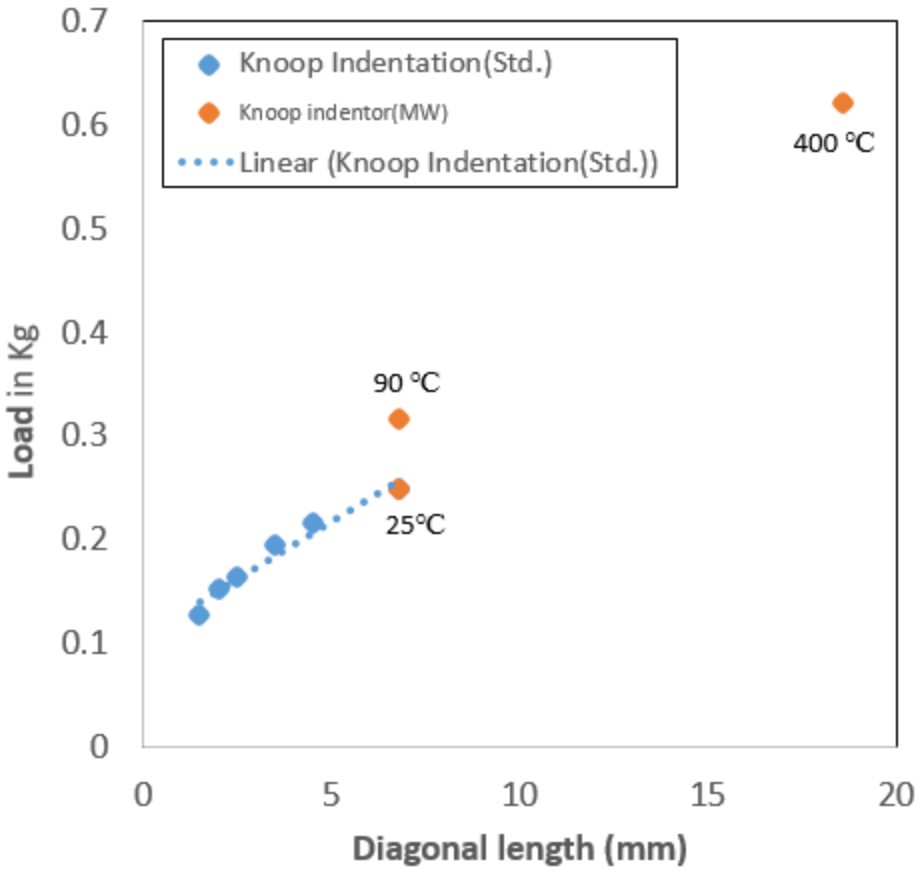

Fig. 12 Knoop indentation data on Al_2O_3:10 wt% $NiFe_2O_4$ measured using standard indentation methods were represented by blue markers, while those measured in the MW chamber (at respective temperatures) were represented by orange markers. The measurement error fell within the size of the marker. The dotted blue line indicated the data trend measured at ambient temperature using the standard system.

Hardness and indentation toughness values of Al_2O_3:10 wt% $NiFe_2O_4$ were successfully measured under MW fields. The data points measured using the MW setup at room temperature followed the linear trends of room-temperature data measured from a standard Knoop indenter, validating the MW measurements. Measured crack length and Knoop hardness (H_K) values from Knoop indents under MW fields at elevated temperatures are shown in Table 3.

Table 3 Crack lengths of Al_2O_3: 10 wt% $NiFe_2O_4$ measured at various temperature and pressure conditions

Run no.	Temperature (°C)	Load (kgf)	Crack length (mm)	H_K (kgf/mm^2)
1	22	6.8	130.5	1572
2	90	6.8	95.5	963
3	400	18.6	707	687

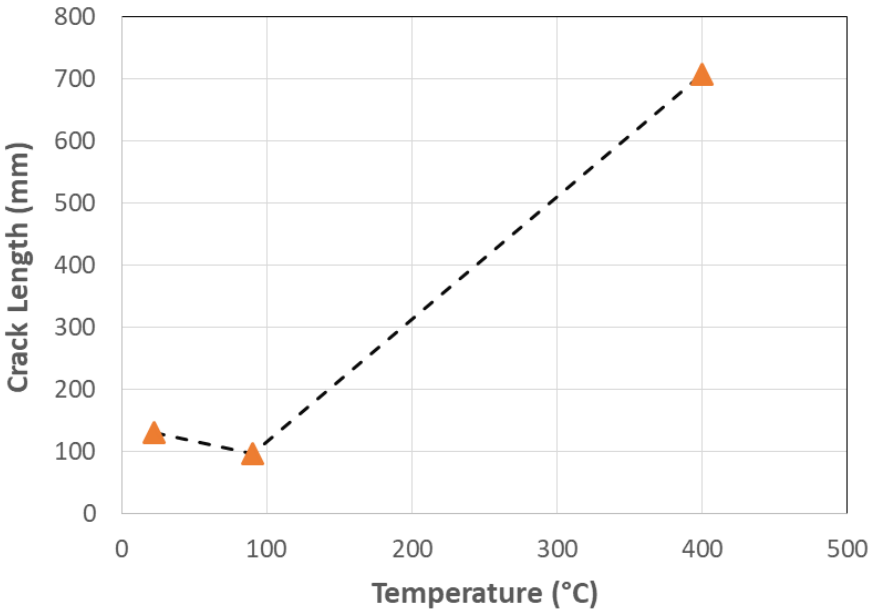

Fig. 13 Crack length of Al_2O_3:10 wt% $NiFe_2O_4$ measured from Knoop indents as a function of temperature. Error bars measured are within the size of the data point.

Figure 13 shows the plot of measured crack lengths as a function of temperature. A decrease in crack length was noted during heating from ambient temperature to 90 °C, indicating that toughening mechanisms were induced by heating under fields. Furthermore, the trend showed an increase in the crack length at 400 °C, indicating a lower toughness than at ambient temperatures. The results from Fig. 13 were consistent with the original idea (based, in part, on preliminary numerical modelling) that toughness was enhanced by the application of external MW fields,[15] indicating the existence of critical temperatures at which toughness decreased due

to crack generation along the particle–matrix interface. More experimental data points are necessary to confirm this theory.

4. Conclusion

Numerical modeling of the crack tip, in relation to the particle size of inclusions, suggested a reduction in stress intensity factor for the largest particles, while the temperature change remained highest. Further, the need for appropriate spacing of the inclusion particles to resist crack propagation was determined. Instrumentation for in-situ indentation under MW fields was designed and implemented. An indentation procedure for Al_2O_3:10 wt% $NiFe_2O_4$ at temperatures up to 400 °C was developed. Initial results indicated consistency with the proposed hypothesis that CTE mismatch stress triggered by applied external MW fields was beneficial to enhancing indentation toughness in ceramics. However, it was difficult to reach and maintain the desired load using the manual hydraulic pump during experimental runs. Hence, it was not possible to collect enough data at the desired constant loads to validate the indentation results obtained at high temperatures. Currently, a process is being developed to incorporate an Instron component into the single-mode MW system to precisely control the applied load and compare the intrinsic effect of MW fields on the toughness of materials under similar load conditions. Additionally, due to consideration of graphitization issues at elevated temperatures, sapphire and/or other super-hard materials that are transparent to MWs will be utilized. This technique may have broader implications for understanding field interactions of materials and their influence over mechanical properties (i.e., fracture toughness), and the underlying mechanisms of materials at high heating rates (e.g., several 100 °C/min) under MW fields.

5. References

1. Zhou H, Pei Y, Huang H, Zhao H, Li F, Fang D. Multi-field nanoindentation apparatus for measuring local mechanical properties of materials in external magnetic and electric fields. Rev Sci Instrum. 2013;84:063906.
2. Duan ZC, Hodge AM. High-temperature nanoindentation: new developments and ongoing challenges. J Minerals Metals Materials Soc. 2009;61(12):32–36.
3. Hernandez T, Rocha-Rangel E. Synthesis, microstructural analysis and mechanical properties of alumina-matrix cermets. Mater Tech Anyagtechnologia 2010;62:2–5.
4. Zhou H, Zhang H, Pei Y, Chen H-S, Zhao H, Fang D. Scaling relationship among indentation properties of electromagnetic materials at micro- and nanoscale. Appl Phys Lett. 2015;106:081904.
5. Wheeler JM, Armstrong DEJ, Heinz W, Schwaiger R. High temperature nanoindentation: the state of the art and future challenges. Curr Opin Solid State Mater Sci. 2015;19:354–366.
6. Quinn GD. Fracture toughness of ceramics by the Vickers indentation crack length method: a critical review. Ceramic Engineering and Science Proceedings; 2006 Jan; Cocoa Beach, FL.
7. Ighodaro OL, Okoli OI. Fracture toughness enhancement for alumina systems – a review. Int J Appl Ceram Technol. 2008;5(3):313–323.
8. Blair VL, Raju CV, Kornecki M, Brennan RE. Single mode microwave sintering of traditionally resistant ceramic materials. Aberdeen Proving Ground (MD); Army Research Laboratory (US); 2017. Report No.: ARL-TR-8466.
9. Seo SY, Mishra D, Park CY, Yoo SH, Pak YE. Energy release rates for a misfitted spherical inclusion under far-field mechanical and uniform thermal loads. Euro J Mech A Solids. 2015;49:169–82.
10. Dassault Systèmes. ABAQUS 6.14 user's manual. Providence (RI): Dassault Systèmes; 2014.
11. Cherepanov GP. Crack propagation in continuous media: PMM. J App Math Mech. 1967;31(3):503–12.
12. Rice JR. A path independent integral and the approximate analysis of strain concentration by notches and cracks. J App Mech. 1968;35(2):379–86.

13. Roy R, Peelamedu R, Hurtt L, Cheng J, Agrawal D. Definitive experimental evidence for microwave effects: radically new effects of separated E and H fields, such as decrystallization of oxides in seconds. Mat Res Innovat. 2002;6:128–140.

14. Knoop F, Peters CG, Emerson WB. A sensitive pyramidal-diamond tool for indentation measurements. J Res Natl Bureau Stand. 1939;23(1):39–61. Research Paper RP1220.

15. Shreiber D, Raju SV, Gray D, Powers B, Pittari J, Blair V, LaSalvia J. Oral presentation at International Conference on Advanced Structural and Functional Materials. EMN 2 ICAS; 2019 Aug 19–23; Barcelona, Spain.

List of Symbols, Abbreviations, and Acronyms

2D	2-dimensional
Al	aluminum
Al_2O_3	alumina
$CoFe_2O_4$	cobalt ferrite
CTE	coefficient of thermal expansion
E	electric
E/H	electric and magnetic field ratios
ECM	energy-coupled-to-matter
EDS	energy dispersive X-ray spectroscopy
EM	electromagnetic
Fe	iron
Fe_2O_3	iron oxide
H	magnetic
MW	microwave
$NiFe_2O_4$	nickel ferrite
NiO	nickel(II) oxide
SiC	silicon carbide
Ti	titanium

1 (PDF)	DEFENSE TECHNICAL INFORMATION CTR DTIC OCA
1 (PDF)	CCDC ARL FCDD RLD DCI TECH LIB
9 (PDF)	CCDC ARL FDCC RLW ME V BLAIR M KORNECKI S KILCZEWSKI B GAMBLE D GRAY S SILTON B LOVE E CHIN J ZABINSKI